BAR

Digital Belt and Road

The 5th Digital Belt and Road Conference

墙报展示

2021/9/6-8 Beijing China

2021年可持续发展大数据国际论坛
International Forum on Big Data for Sustainable Development Goals
2021/9/6-8 中国·北京

柬埔寨电能消耗和夜光总值的耦合模型助力数字一带一路计划

高许淼[1,2]，邬明权[1*,2]
（1. 中国科学院空天信息创新研究院，北京 100094；
2. 中国科学院大学，北京 101408；）

联合国可持续发展目标指出到 2030 年确保每个人都能获得负担得起、可靠、可持续和现代的能源。然而，一带一路协议国普遍面临着电能短缺的问题。正确估计一带一路协议国的电能消耗及其时空格局的动态变化，对电能规划具有重要意义。夜光遥感数据与电能消耗具有高度相关性，可为一带一路协议国的电能消耗估算提供参考。以柬埔寨为例，研究了多云多雨地区用电量的夜光遥感估算方法。利用 NPP/VIIRS 月平均夜光影像数据通过三种方式合成柬埔寨的年发光图像:全年平均法、无云平均法，特定月份代替法，并对三种方法得到的年夜光影像进行投影、重采样、去噪等处理。将处理后柬埔寨年夜光影像的夜光总量分别与柬埔寨的年用电量数据进行不同函数模型的耦合回归分析。结果表明:(1)柬埔寨年夜光影像发光总量和耗电量数据强相关性。(2)三种不同方法合成柬埔寨年夜光影像质量为:全年平均法<无云平均法<特定月份代替法。(3)柬埔寨夜光总量和耗电量数据之间的最佳耦合为指数模型。本研究展示了柬埔寨夜光总值与用电量之间的强相关性，为合成多云多雨地区的年夜光影像提供了新思路。在此基础上，估算了柬埔寨的年用电量，分析了 2012-2019 年柬埔寨用电量的时空格局变化。本文计算了柬埔寨电力消费的时空数据，将有助于一带一路协议国实现联合国可持续发展目标 7 和协助数字一带一路计划。

DBAR-06

2021年可持续发展大数据国际论坛
International Forum on Big Data for Sustainable Development Goals
2021/9/6-8 中国 · 北京

Water availability surpasses warmth in controlling global vegetation trend

Anzhi Zhang, Gensuo Jia
CAS Key Laboratory of Regional Climate-Environment for Temperate East Asia, Institute of Atmospheric Physics, Chinese Academy of Sciences, Beijing, China

Satellite-derived vegetation indices enable quantification of global vegetation productivity changes, and indicate heterogeneous regional trends with an overall greening trend and an increased browning trend (slowdown or reversal of greening) in recent years. However, the detailed spatial-temporal evolutions and the climatic drivers that effect vegetation trends are not well

Recent reversal of vegetation greening and carbon uptake

Trends in vegetation greening and terrestrial carbon uptake reverse in the early 2000s, largely driven by the recent drying trend.

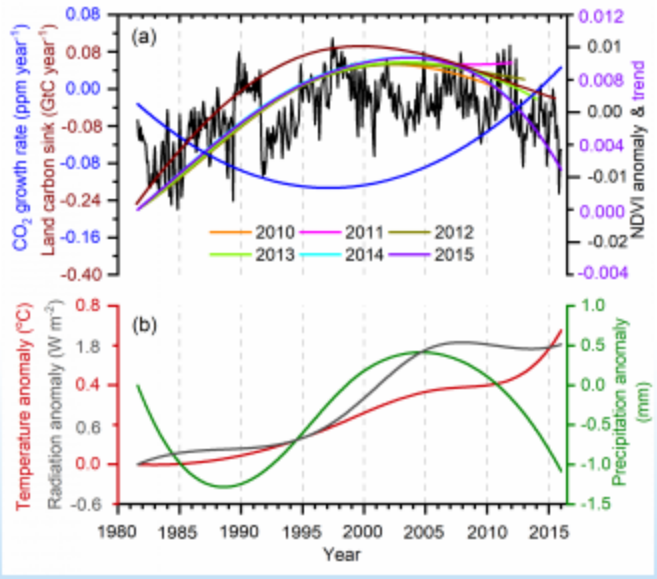

Fig 1. Covariation in the time-varying trend of vegetation

Contributions of regional to global vegetation trend

The Northern Hemisphere (88.6%) controls the global vegetation trend from 1981 to 2015. Biomes of croplands (23.5%) and grasslands (23.5%) dominate the vegetation greening trends.

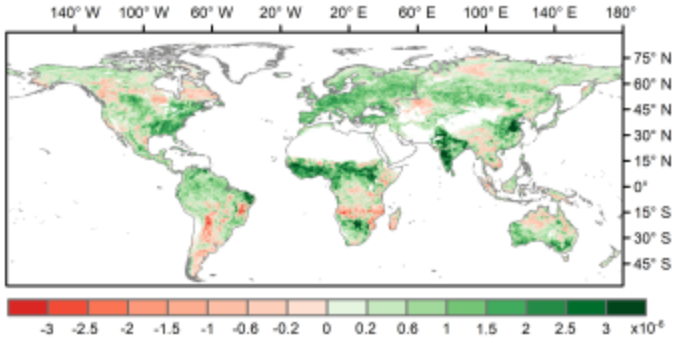

Fig 2. Contributions of regional to the global vegetation productivity trend in space.

Weakening temperature, strengthening precipitation control

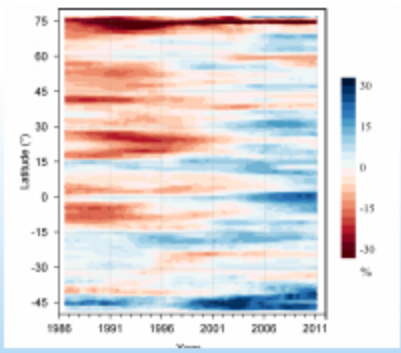

Fig 3. The spatial-temporal relative importance of climatic control of precipitation and temperature. **Blue: precipitation dominance.**

The dominant climatic driver of vegetation trend shifts from temperature to precipitation, and point to intensified water limitation to vegetation growth as warming continues.

This work was supported by the Strategic Priority Research Program of the Chinese Academy of Sciences (XDA19030401).
Contact Author: Gensuo Jia, jiong@tea.ac.cn

FBAS
2021年可持续发展大数据国际论坛
International Forum on Big Data for Sustainable Development Goals
2021/9/6-8 中国 · 北京

Monitoring the spatiotemporal variation of Siberian crane habitats in Poyang Lake wetland, China

Lin Zou[1], Bisong Hu[1], Shuhua Qi[2], Qianqian Zhang[1], Pan Ning[1]
[1]School of Geography and Environment, Jiangxi Normal University, Nanchang, China
[2]Key Laboratory of Poyang Lake Wetland and Watershed Research, Ministry of Education, Jiangxi Normal University, Nanchang, China
Contact Author: Bisong Hu, hubisong@jxnu.edu.cn

The Poyang Lake wetland in China is the largest wintering destination for the Siberian crane, which is one of the critically endangered species. Approximately 98% of wintering Siberian cranes migrate from their breeding grounds to the Poyang Lake wetland area. The hydrological situation of Poyang Lake is the main influence factor that determines the quality of Siberian crane habitats. Monitoring the spatiotemporal variation of Siberian crane habitats in the past 30 years is an effective support to SDG 15.5, which includes reducing the degradation of natural habitats and others. It is of great significance for ecological environment protection and management of the Poyang Lake wetland to study the spatiotemporal variation of Siberian crane habitats, their corresponding response to water level changes and the potential impacts of human disturbances on the habitats.

This study demonstrates the technical process of remote sensing classification of the crane habitats and the corresponding methods of monitoring their spatiotemporal variation, including landscape metrics, spatial statistics and vulnerability indicators. The findings indicate: *i*) The hot spots of the habitats formed multiple "sheet" belts centered on the "Lake Enclosed in Autumn" regions of the sub-lakes on the east and west banks of the Poyang Lake, whereas the cold spots were mainly distributed in the main channels of the basins of Poyang Lake. *ii*) The sustainable crane habitats were intensively aggregated in the areas of Nanjishan and Wucheng national nature reserves, and an increase of water level will cause a decrease of the stability and variety of the habitats and weaken their aggregation structure.

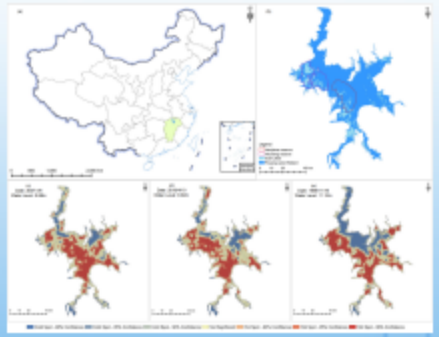

(a) The hot/cold spots of the habitas

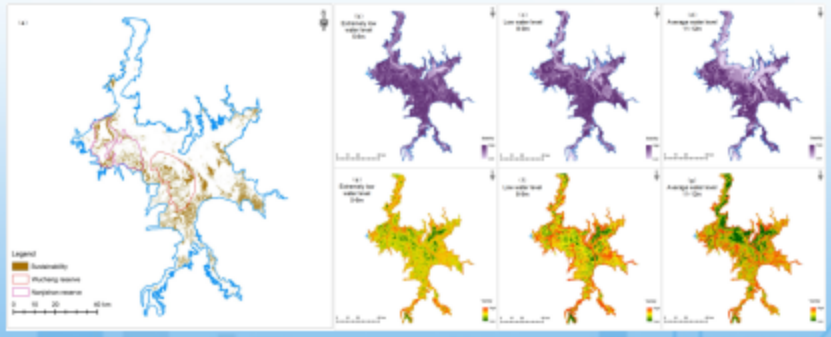

(b) Vulnerability distributions of the crane habitats

DBAR-11

2021年可持续发展大数据国际论坛
International Forum on Big Data for Sustainable Development Goals
2021/9/6-8 中国·北京

The global long-term vegetation dynamics inferred from satellite optical and microwave observations

Minhua Wang[1,2], Anzhi Zhang[1] Contact: wangmh@tea.ac.cn zhanganzhi@tea.ac.cn

[1] CAS Key Laboratory of Regional Climate-Environment for Temperate East Asia, Institute of Atmospheric Physics, Chinese Academy of Sciences, Beijing, China

[2] Beijing Forestry University, Beijing, China

Introduction

Terrestrial vegetation plays a central role in mitigating human-induced climate change. The satellite derived vegetation indices can monitor the global terrestrial vegetation change, and they are widely used to indicate vegetation greening or browning. Most studies have investigated the dynamics of vegetation trend based on satellite optical remote sensing derived vegetation indices, such as the normalized difference vegetation index (NDVI), However, it is susceptible to atmospheric influences (e.g., aerosols and cloud) and limited to monitoring the top of the canopy. The vegetation optical depth (VOD), retrievals from satellite passive microwave observations, can monitor vegetation dynamics, both leaf and woody components of aboveground living biomass.

Annual Average

NDVI and VOD shows similar spatial patterns, and both of them have higher values over tropical regions and 50° N.

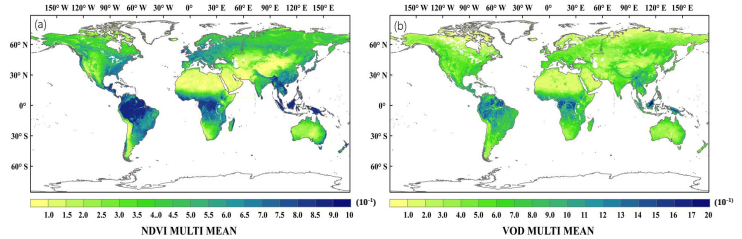

Fig. 1 | Climatology of global normalized difference vegetation index (a) and vegetation optical depth (b).

Biome Distribution

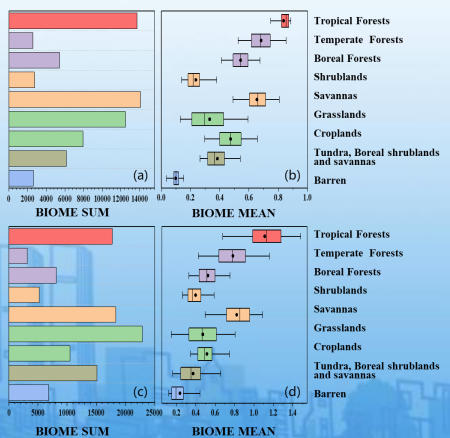

The images show that forests have the highest density of VOD and NDVI, especially tropical rainforests. And, forests and grasslands have the highest total. In addition, savannas have high densities and total volumes.

Fig. 2 | Global NDVI total value (a) and density(b);Global VOD total value (c) and density(d).

Greenness Changes

Using the NDVI and VOD time series from 1988-2015, we found significant vegetation greening over the past 28 years, and the VOD shows significantly stronger greening trend than that of NDVI. In addition, the trend varies across ecoregions, in particular over forests in the middle and low latitudes, between the two indices.

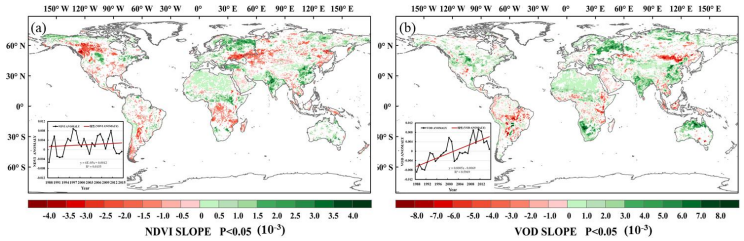

Fig. 3 | Changes in global Normalized difference vegetation index(a) and vegetation optical depth(b) .

Biome Trend

The NDVI shows a stronger browning trend than that of VOD. In addition, temperate forests and savannas exhibit contrast trend between VOD (greening) and NDVI (browning).

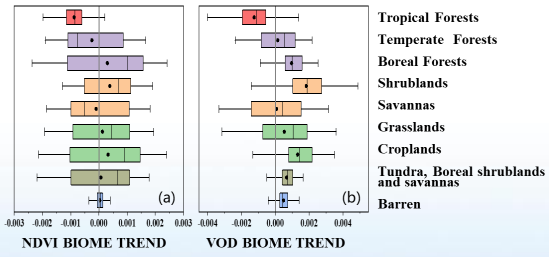

Fig. 4 | Annual trends in total biome for 1988–2015 Normalized difference vegetation index(a) and vegetation optical depth(b) .

Discussion

The satellite microwave derived vegetation optical depth can penetrate the canopy, and it is more sensitive to changes in biomass across all biomes. However, the satellite optical derived normalized difference vegetation index measures the greenness of the canopy surface. Therefore, the contrast trends of forest and savannas of VOD and NDVI are tightly related to the above mentioned characteristics of microwave and optical remote sensing. It is better to use both the indices to obtain a more robust understanding of the long-term vegetation changes.

2021年可持续发展大数据国际论坛
International Forum on Big Data for Sustainable Development Goals
2021/9/6-8 中国·北京

Scenarios simulation of the Change of Terrestrial Carbon Storage and Carbon Emissions under the constraints of multiple SDGs indicators

Introduction

Land use affects the environment by changing the terrestrial ecosystem, and its pattern change is the basis for studying the carbon storage and carbon emissions of the terrestrial ecosystem. Based on the four development scenarios of reference, economy, environment and society under the constraints of multiple SDGs, coupled with the System Dynamics-Cellular Automata-Integrated Valuation of Ecosystem Services and Trade-offs (SD-CA-InVEST) model, this research uses the carbon emission coefficient method to simulate the carbon storage and carbon emissions of terrestrial ecosystems under multiple scenarios in China in the past and the future from the perspective of land use, and explore their spatial differentiation.

Method

Result

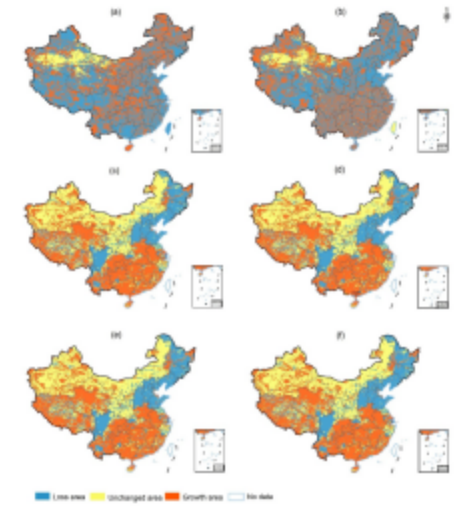

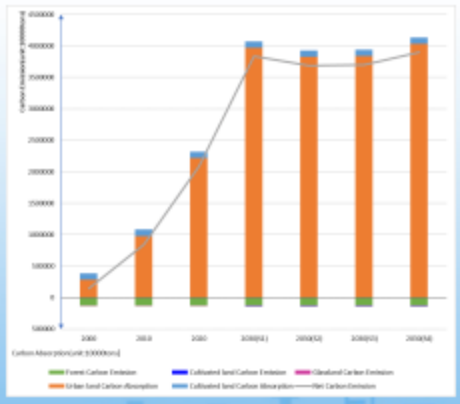

Conclusion

From 2000 to 2030, the total carbon emissions and net carbon emissions have shown an increasing trend, which reaches its peak in 2030. Under the next four scenarios, the growth of carbon storage will be concentrated in my country's Qinghai-Tibet Plateau and southern regions, while the reduction areas are mainly distributed in the Northeast, North China and Sichuan Basin, and there is little change in Northwest China.

Hu Xue Key Lab of Virtual Geographic Environment, Ministry of Education of PRC, Nanjing Normal

2021年可持续发展大数据国际论坛
International Forum on Big Data for Sustainable Development Goals
2021/9/6-8 中国·北京

Urban natural environment is an important factor affecting the incidence of lung cancer, while urban built environment, such as urban traffic, land use, and architectural form also have an influence on the living environment and lifestyle of urban residents, and increasingly significant impact on the incidence of lung cancer. With a certain district, Bengbu City, Huaihe River Basin, China as the study area, to explore the basic characteristics of lung cancer patients from 2010-2020, we discussed the basic characteristics of lung cancer patients from 2010-2020, analyzed the risk factors of urban environment on the death risk of lung cancer patients through Cox proportional hazard model, and selected the affected population from 2018-2020 to build an index system of urban multiple environmental factors through Spearman to analyze the influence path of urban environmental factors on lung cancer. The results showed that: (1) Lung cancer mainly occurred in the middle-aged and elderly in the YH08 unit of study area, and the population distribution was characterized by aggregation. (2) Land use, road traffic, spatial form, and service facilities in urban built environment, air pollution, temperature, green space and open space in natural environment were all correlated with the incidence of lung cancer. (3) In Cox proportional hazard model, building density, vegetation coverage index and SO_2 are the risk factors of lung cancer death. The optimization suggestions were put forward for the incidence of lung cancer based on the study results, and appropriate urban planning and policies could be taken to reduce the incidence of lung cancer.

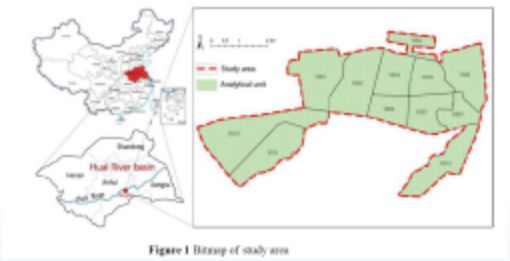

Figure 1 Bitmap of study area

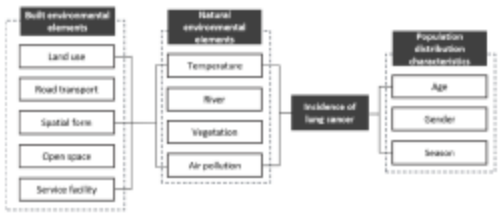

Figure 2 Frame diagram

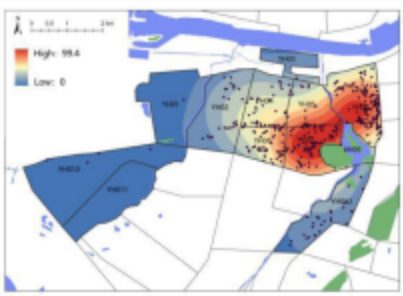

Figure 3 Spatial distribution analysis of lung cancer incidencepopulation in a certain district of Bengbu City from 2010-2020

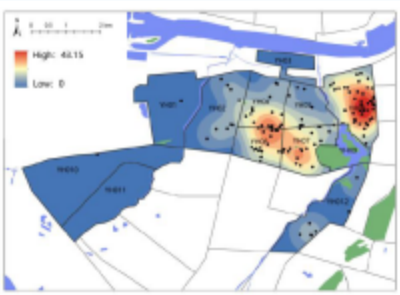

Figure 4 Spatial distribution analysis of lung cancer incidencepopulation in a certain district of Bengbu City from 2018-2020

DBAR-15

2021年可持续发展大数据国际论坛
International Forum on Big Data for Sustainable Development Goals
2021/9/6-8 中国 · 北京

OPTIMIZING A NETWORK OF DRONE-AIDED HEALTHCARE SERVICES IN RURAL RWANDA

Chinasa I. Ikelu[1], Eugene C. Ezin[2]

[1] Institut de Mathematiques et de Sciences Physiques (IMSP), Dangbo, Benin Republic

[2] Institut de Formation et de Recherche en Informatique (IFRI), University of Abomey Calavi, Benin Republic

Background

Transporting health care products from one point to another using innovative technology like drones can be difficult to achieve especially in hard-to-reach areas in rural Rwanda. This study focuses from the start of drone operation in Rwanda until 2018. We observed that data is critical to the success of any facility location analysis.

Methods

Minimize $\sum_{i\epsilon I} f_{ij} \sum_{j\epsilon J} X_{ij}$

Subject to:

$\sum_{i=1}^{n} X_{ij} \leq S_i$

$\sum_{j=1}^{m} X_{ij} \geq D_j$

$X_{ij} \geq 0$

$X_{ij} - C_i * t_r \leq 0$

$C_i * (t_r - 1) \leq X_{ij}$

$t_r \geq 0$

$t_r \leq X_{ij}$; $\forall\, i = 1, \ldots, n; \forall\, j = 1, \ldots, m$

Aims/Objectives

We envisage that drone-aided health care services can reduce the shipping costs associated with transporting blood from the plants to the centers and that the time it will take to delivery such health care product to their various destinations can be minimized as well.

***German Academic Exchange Service (DAAD)**

Findings

N = 2	M = 12 (value for y)											
	1	2	3	4	5	6	7	8	9	10	11	12
1	1	1	1	1	1	1	1	1	1	1	1	1
2	0	0	1	0	0	0	0	0	0	0	0	0

N = 2	M = 12 (value for x)											
	1	2	3	4	5	6	7	8	9	10	11	12
1	54	30	13	41	97	11	62	59	35	42	19	12
2	0	0	30	0	0	0	0	0	0	0	0	0

Conclusions

Drone-aided networks using simulation analysis and a numerical optimization model helps in obtaining the optimal cost-effective point associated with transporting blood in Rwanda and finding an optimal solution to the agent and input-output based models.

DBAR-18

2021年可持续发展大数据国际论坛
International Forum on Big Data for Sustainable Development Goals
2021/9/6-8 中国 · 北京

Long-term hydrometeorological and snow observations in the Tianshan Mountains, Xinjiang China

Lanhai Li[1,2,3,4], Qian Li[1,2,4], Yang Liu[1,2,3,4]

[1]State Key Laboratory of Desert and Oasis Ecology, Xinjiang Institute of Ecology and Geography, Chinese Academy of Sciences, Urumqi 830011, China;

[2]Ili Station for Watershed Ecosystem Research, Chinese Academy of Sciences, Xinyuan 835800, China;

[3]CAS Research Centre for Ecology and Environment of Central Asia, Urumqi 830011, China;

[4]Xinjiang Key Laboratory of Water Cycle and Utilization in Arid Zone, Urumqi 830011, China.

Mail: lilh@ms.xjb.ac.cn Tel: +86-991-7823160

Tianshan Station for Snow-cover and Avalanche Research (TSSAR), established in 1967, is located in the western section of the Tianshan mountains at latitude 43° 16′ N and longitude 84° 24′ E with an elevation of 1776 m above sea level. The Tianshan Mountains have a typical continental snow climate. According to long term observation, the mean annual temperature at the TSSAR is approximately 1.4°C, while average annual precipitation is 870 mm and solid precipitation in the cold season accounts for more than 30% of annual precipitation. Average snow depth in the station is 78 cm and annual Snow-cover days are 150 Days. Meteorological and hydrological data are monitored from an observation network connecting a group of automatic meteorological stations. In addition, we have started a daily manual snow pit observation since 2017 during entire snow season, which contains snow depth, snow layer density, snow layer temperature, and layer water content. The current study at this station focuses on the fundamental studies on patterns and processes related to snow resources service functions, snow hydrology and disaster prevention. It is important for freshwater utilization and management, as well as the construction and conservation of ecological safety barriers in the alpine region.

DBAR-19

2021年可持续发展大数据国际论坛
International Forum on Big Data for Sustainable Development Goals
2021/9/6-8 中国·北京

Analysis of sea surface temperature variation in the Northeast Passage in the past 30 years

Yang Meng[1 2], Qiu Yubao[2*], Huang Lin[2 3], Cheng Maoce[1 2], Chen Jianguo[1]

[1] Sch Earth Resources, China University of Geosciences, Wuhan, China

[2] Aerospace Information Research Institute, Chinese Academy of Science(AIR-CAS), Beijing, China

[3] College of Resources and Environment, University of Chinese Academy of Sciences, Beijing, China

ABSTRACT

Global warming has created favorable conditions for the utilization of Arctic Passage. Sea surface temperature (SST) not only promotes the melting of sea ice, but also has an important effect on the ocean-atmosphere interaction. In this study, for the period from May to December of 1990–2020, we analyzed the temporal and spatial characteristics of SST variation in the Northeast Passage (NEP). The long term analysis shows monthly mean SST is highest in August and warming trends of SST in the NEP, especially in August (0.079 ℃ /year). In addition, we analyzed the correlation between SST and sea ice concentration (SIC) in the NEP from 2002 to 2020.

INTRODUTION

A lot of studies on the SST patterns of Arctic Ocean and the potential relationship between SST and climate variables. The melting of sea ice caused by the warming of SST has a great impact on Arctic shipping and the change of navigation window. SST in the NEP is therefore of considerable significance.

DATA AND PROCESSING

The AMSR-E/AMSR2 daily sea ice concentration data from 2002 to 2020 was released by the University of Bremen (https://seaice.uni-bremen.de/data). The NOAA 1/4°daily Optimum Interpolation SST (OISST Version 2.1) from 1990 to 2020 was obtained from the National Centers for Environmental Information (NCEI) (https://www.ncei.noaa.gov/).

Monthly SST from May to December of 1990–2020 was a month average of daily OISST and the linear fitting method was applied for trend estimation. Correlation analysis between SST and SIC in the NEP from 2002 to 2020.

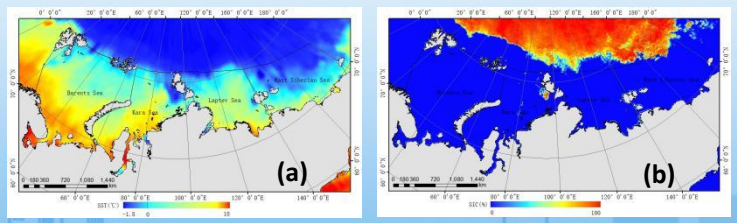

Figure 1. SST (a) and SIC (b) of 2020/08/15 in the NEP

RESULTS

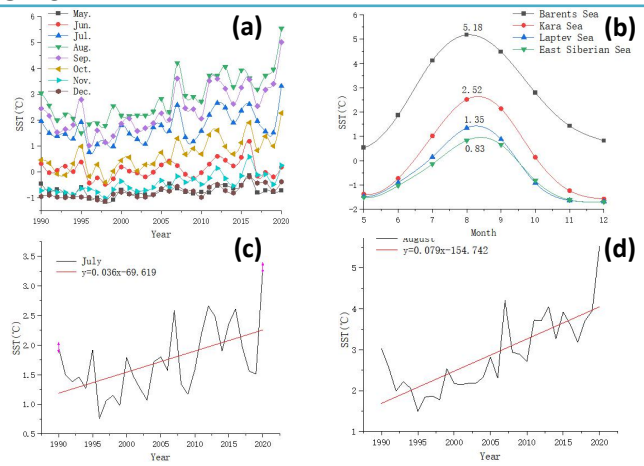

Figure 2. Statistics of Monthly SST (a) and mean monthly SST of four regions (b) from May to December of 1990-2020 in the NEP. July (c) and August (d) linear

Table 1. Annual monthly SST trends of 1990-2020 in the NEP

	May.	Jun.	Jul.	Aug.	Sep.	Oct.	Nov.	Dec.
℃/year	0.008	0.001	0.036	0.079	0.072	0.052	0.030	0.020

Table 2. Correlation coefficient r of SST and SIC of 2002-2020 in the NEP

Correlation	NEP	Barents	Kara	Laptev	East Siberian
r	-0.917	-0.791	-0.878	-0.891	-0.882

SST has been increasing from 1990 to 2020 (table 1), especially in August (0.079 ℃ /year). The SST and SIC show negative significant correlation during 2002-2020 in the NEP (table 2).

CONCLUSION

(1) The monthly SST of Barents Sea was the highest, followed by Kara Sea, Laptev Sea and East Siberian Sea for 1990-2020 in the NEP. The highest monthly SST (2.87℃) and annual warming trend of SST (0.079℃/year) in the NEP appeared in August. This may lead to the advance and extension of the navigation window of Arctic shipping.

(2) The SST and SIC show negative significant correlation for 2002-2020 in the NEP. The correlation of SST-SIC in the Laptev Sea was the strongest, however, in the Barents Sea is weaker.

Support Grant: the National Key Research and Development Program of China No.2019YFE0105700)

REFERENCE

Huang, B., C. Liu, V. Banzon, E. Freeman, G. Graham, B. Hankins, T. Smith, and H.-M. Zhang (2021), Improvements of the Daily Optimum Interpolation Sea Surface Temperature (DOISST) Version 2.1. J. Climate, 34, 2923-2939, doi:10.1175/JCLI-D-20-0166.1

Spreen, G., L. Kaleschke, and G.Heygster (2008), Sea ice remote sensing using AMSR-E 89 GHz channels J. Geophys. Res.,vol. 113, C02S03, doi:10.1029/2005JC003384.

DBAR-20

2021年可持续发展大数据国际论坛
International Forum on Big Data for Sustainable Development Goals
2021/9/6-8 中国·北京

Characteristics Analysis of Precipitation Variables in the Northeast Passage of Arctic

Cheng Maoce [1,2], Qiu Yubao [2], Yang Meng [1,2], Huang Lin [2,3], Chen Jianguo [1]

1 Sch Earth Resources, China University of Geosciences, Wuhan, China
2 Aerospace Information Research Institute, Chinese Academy of Science(AIR-CAS), Beijing, China
3 College of Resources and Environment, University of Chinese Academy of Sciences, Beijing, China

Abstract: Arctic precipitation causes changes in sea ice through surface albedo, it affects the energy exchange between the sea ice, the atmosphere and sea ice Growth. Accurate precipitation is very important for the Arctic area. Use the global coverage of 0.1° spatial resolution GPM IMERG precipitation data to study the precipitation characteristics of the Northeast Passage(NEP) from May to December during 2011 to 2020, comparing and analyzing the precipitation in the Arctic ocean and inland areas (60° to the coastal zone), including the Barents Sea, Kara Sea, Laptev Sea, East Siberian Sea and the coastal zone's precipitation distribution, precipitation size. The results show that the average total precipitation in the Barents Sea is the largest in the NEP, while the average total precipitation in the Eastern Siberian Sea and the Laptev Sea is relatively small. The precipitation is mainly concentrated in the Barents Sea and Kara Sea,this may be related to some tropical water vapor entering the Arctic.Through the correlation analysis of precipitation, sea ice concentration and moisture data in recent ten years, it is found that precipitation is positively correlated with moisture and negatively correlated with sea ice concentration, which is closely related to the navigation capacity of the Northeast passage.

Data & Research Area

Data : GPM IMERG Final Precipitation L3 1 day 0.1x0.1 degree V06
Data Time Range : 20110501-20201231 ; Time Resolution:1 day
Data Space Range : -180.0°, 60.0°,180.0°,90.0° ; Unit:mm

The Northeast Passage (NEP) is one of the crucial Arctic routes, it can save the voyage from Western Europe to North east Asia, which traverses the Barents, Kara, Laptev and East Siberian sea. The research area include the NEP and the land of 60°N to coastal zone.

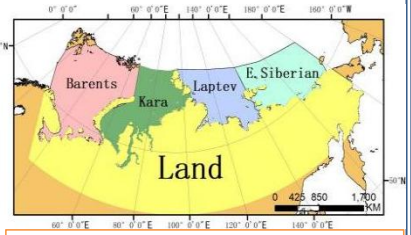

Fig.1 Research Area

Result

According to Fig.2, the NEP precipitation from high to low is the Barents, Kara, Laptev and East Siberian Sea. The inland areas of Barents and Kara Sea have larger precipitation,while the inland areas of Laptev and East Siberian Sea have less precipitation.

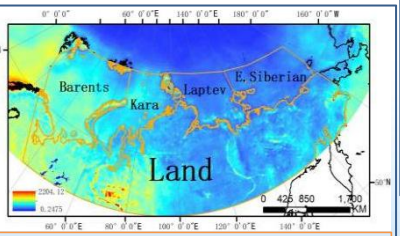

Fig.2 Average annual precipitation in the study area from 2011 to 2020

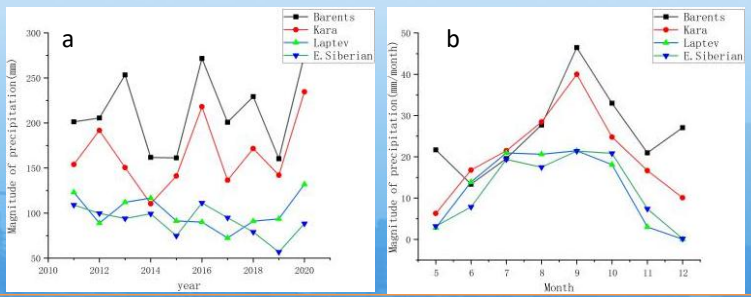

Fig.3 (a) Broken line chart of annual precipitation in each sea area.
(b) Broken line chart of average monthly precipitation in each sea area

The annual precipitation of the Barents Sea and Kara Sea can reach 200-300mm,while the Laptev and East Siberian Sea is about 150mm (Fig.3a). The maximum precipitation is concentrated in August and September in the NEP (Fig.3b) because of increasing precipitation in the Barents and Kara Sea.

Tab.1 Correlation coefficient between Sea Ice Concentration (SIC), Moisture and Precipitation each area

Area	NEP	Barents	Kara	Laptev	E.Siberian
Moisture	0.41	0.07	0.49	0.72	0.24
SIC	-0.79	-0.33	-0.77	-0.84	-0.52

According to Tab.1, precipitation has a impact on SIC and moisture. There is a positive correlation between precipitation and moisture while the largest correlation in the Laptev Sea and the smallest correlation in the Barents Sea.A negative correlation occurs between precipitation and SIC while the largest correlation in the Laptev Sea and the smallest correlation in the Barents Sea. The moisture entering the Arctic will increase the precipitation in the Northeast passage , and the increased precipitation will reduce the sea ice concentration in the passage area so that the Northeast passage can be navigable.

Conclusion

(1) The precipitation distribution in the NEP is high in the West and low in the East and the precipitation is distributed in the estuary and coastal zone.The monthly average precipitation of the Northeast passage increases first and decreases then, the precipitation is the largest in September. The Barents Sea and Kara Sea contribute greatly to the precipitation from August to September.
(2) According to correlation coefficient,moisture leads to the increase of precipitation, but the precipitation reduces the SIC, which is beneficial to the navigation of the Northeast passage.

Support Grant: the National Key Research and Development Program of China (No.2019YFE0105700)

Reference
[1]Boisvert, L.N., et al., Intercomparison of Precipitation Estimates over the Arctic Ocean and Its Peripheral Seas from Reanalyses. Journal of Climate, 2018. 31(20): p. 8441-8462.
[2]Barrett, A.P., J.C. Stroeve and M.C. Serreze, Arctic Ocean Precipitation From Atmospheric Reanalyses and Comparisons With North Pole Drifting Station Records. Journal of Geophysical Research: Oceans, 2020. 125(1).

DBAR-21
2021年可持续发展大数据国际论坛
International Forum on Big Data for Sustainable Development Goals
2021/9/6-8 中国·北京

Temporal and Spatial Variation of Surface Energy Flux in permafrost regions on the Qinghai-Tibet Plateau and Arctic Regions Using CMIP6 Models

LI Ren, MA Junjie, WU Tonghua
Cryosphere Research Station on the Qinghai-Tibet Plateau, State Key Laboratory of Cryospheric Science, Northwest Institute of Eco-Environment and Resources, Chinese Academy of Sciences, Lanzhou 730000, China

• 1 Introduction

Permafrost is a key component of the cryosphere, occupying approximately 21.8% of the exposed land area in the Northern Hemisphere (Obu et al., 2019). As a special underlying surface, permafrost stores abundant organic carbon, and it plays an important role in the ground-air exchange, land surface processes, and hydrological cycles (Carvalhais et al., 2014; Mu et al.,2020). Therefore, considering the important role of permafrost in the cryosphere and the entire earth system, permafrost is considered an indicator of climate change (Kang et al., 2010). Significant changes have occurred in the global climate over the past several decades, the global climate experienced a warming trend. For permafrost regions, their warming were considered to have the potential to amplify global climate change (Biskaborn et al., 2019; Mu et al.,2020). As the highest altitude and latitude area in the northern hemisphere, the Qinghai-Tibet Plateau (QTP) and the Arctic have responded more strongly and prominently under the background of global warming (Guo et al., 2016; Pepin et al., 2015). The QTP and Arctic region are more sensitive to climate change and thus become the focus of climate change research. The Coupled Model Intercomparison Project phase 6 (CMIP6, Eyring et al., 2016) provided the latest and most profound coordinated international climate model intercomparison project (Martin, 2020). The differences between CMIP6 models and those of CMIP5 are in those of a new generation models and a different end year (2014 for CMIP6 and 2005 for CMIP5) for the historical experiments (Gidden et al., 2019; Mansour et al., 2020).

• 2 Data and method

The in situ data used in this study were obtained at the Tussock flux tower (149.30W,68.61N) and Tanggula site (91° 52′E; 33° 04′N) (Fig.1). And we also selected 19 models of surface energy flux from the CMIP6 Project in this study.

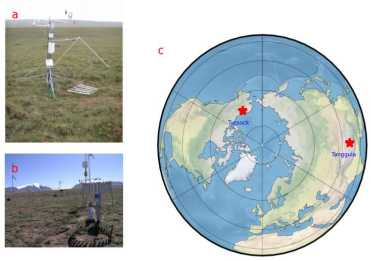

Fig.1 Location of the (a)Tussock flux tower, (b)Tanggula flux tower at the North Hemisphere

The net radiation (*Rn*) was measured with a four-component net radiometer, and it was calculated from the upward shortwave radiation (*RSUS*), upward longwave radiation (*RLUS*), downward shortwave radiation (*RSDS*) and downward longwave radiation (*RLDS*) according to the following equation:

$$Rn = RLDS - RLUS + RSDS - RSUS \quad (1)$$

The ground heat flux (G_0) was calculated according to the following equation:

$$G_0 = G_z + C_s \int_0^z \frac{\partial T}{\partial t} \mathrm{d}z \approx G_z + C_s \frac{\Delta T}{\Delta t} z \quad (2)$$

Where G_Z is the observed soil heat flux (W m^{-2}) at a depth of z cm, z is 5 cm, and C_S is the averaged volume heat capacity (J m^{-3} K^{-1}), additionally, in the north QTP *Cs* values were suggested to be 1.18×10^{6}J ·m^{-3} K^{-1} (Tanaka et al., 2001).

• 3 Results

3.1The performance for surface energy flux in CMIP6 and the comparison with CMIP5

Fig.2 illustrates the temporal behavior of surface energy flux derived from the 19 CMIP6 models compared with the in suit data of the Tangula site in 2007. It implied that the *LE*, *RLDS* and *RLUS* showed a good agreement with in situ data, especially for *RLDS* and *RLUS*, both had a significant positive correlation, and were both above 0.8. More recently, results on CMIP5 showed that the correlation coefficients of the 17 models were all below 0.3, and nearly half of the models with negative correlation (Hu et al., 2019).

Similarly, in the assessment of the Tussock site (Fig. 3), the *LE* showed the best simulation effect of all 19 CMIP6 models, and the correlation coefficient was around 0.8. For *H*, the simulation effect was not as good as *LE*, but it was better than the evaluation result of Tanggula site, the correlation coefficient was around 0.6. For the assessment of net radiation, the 19 models of CMIP6 also showed a good simulation result. And the correlation coefficient of each model was around 0.8.

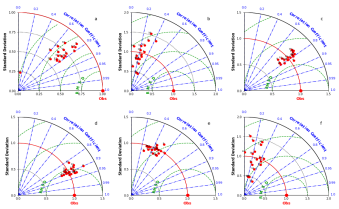

Fig. 2. Taylor program for daily averages of the surface energy flux of (a) *LE*, (b) *H*, (c) *RLDS*, (d) *RLUS*, (e) *RSDS* and (f) *RSUS* between CMIP6 models and observation at Tanggula site in 2007

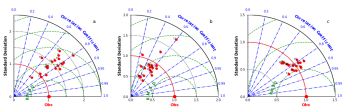

Fig. 3. Taylor program for daily averages of the surface energy flux of (a) *LE*, (b) *H*, (c) *Rn* between CMIP6 models and observation at Tussock site in 2007

3.2 *The average multi-model results evaluation*

Fig. 4, shows the performance of the multi-models in the simulation of surface energy flux over Tanggula in 2007. *Rn* and G_0 were calculated by Eqs.(1) - (2). It was evident, that the multi-models average of *Rn* exhibited the best performance, closely matched the observed value, and the R value reached 0.87. Followed were *LE* and G_0, and the R values also reached above 0.80, 0.83 and 0.81 respectively. The R values of *H* and net longwave radiation were not very ideal, both were below 0.5, with value of 0.4 and 0.36 respectively. It was noteworthy that from the degree of dispersion in Fig. 4, the performance of *Rn*, net shortwave and net longwave radiation were more concentrated and close to the observed value. Also, we compared the multi-model simulation results over the Tussock station (Fig. 5). Similar to the results at Tanggula site, *Rn* also showed the best simulation effect, followed by *LE*. Relatively speaking, the simulation result of *H* in Tussock station was better than that of Tanggula site. As a whole, the results of CMIP6 can reasonably represent the characteristics of surface energy flux.

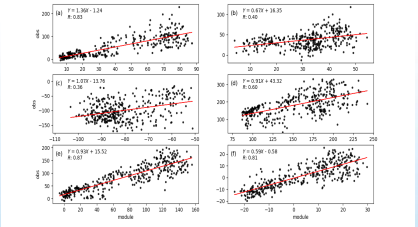

Fig. 4. Land surface heat flux simulated by the average multi-model ensemble vs. observed: (a) latent heat flux, (b) sensible heat flux, (c) net longwave radiation heat flux, (d) net shortwave radiation heat flux, (e)net radiation heat flux and (f) soil surface heat flux at Tanggula site in 2007.

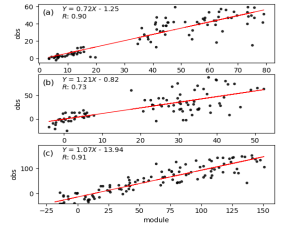

Fig. 5. Land surface heat flux simulated by the average multi-model ensemble vs.observed: (a) latent heat flux, (b) sensible heat flux, (c)net radiation heat flux and at Tussock site in 2007

• 4 Conclusion

The surface energy flux of 19 CMIP6 models at Tanggula site and Tussock had been assessed. The evaluation results in this study revealed that the majority in CMIP6 models for *LE* and *Rn* were close to the in situ data, with correlation coefficients around 0.80. And the simulation results of CMIP6 in the Arctic region were better than those in the QTP. Overall, the average multimodel ensemble can represent the surface energy flux characteristic over the QTP and the Arctic region. Besides, compared with CMIP5, the simulation performance of CMIP6 had been greatly improved.

2021年可持续发展大数据国际论坛
International Forum on Big Data for Sustainable Development Goals
2021/9/6-8 中国 · 北京

Surging Dynamics of South Rimo Glacier, Eastern Karakoram

Kunpeng Wu[1], Shiyin Liu[1], Zongli Jiang[2]
[1]Institute of International Rivers and Eco-Security, Yunnan University, Kunming, 650091, China
[2]Hunan University of Science and Technology, Xiangtan, 411201, China

Abstract

A comprehensive suite of surface velocities and surface elevation changes for the surging South Rimo Glacier (SRG), situated in the East Karakoram region, are obtained by offset-tracking from Sentinal-1A and geodetic method from TerraSAR-X/TanDEM-X and ICESat-2 ATLAS. The surge of SRG initiated in the summer of 2018, and the rapid and dramatic increase in surface velocities reached a peak (~12 m d^{-1}) in August 2019. By the summer of 2020, the surface velocity of SRG had returned to its pre-surge level. We interpret that the evolution of the latest SRG surge was probably triggered by changes in subglacial thermal conditions, and was ultimately accelerated by hydrological processes. Based on historical analysis, a surge return period of ~25-30 years prevails at SRG.

Data and methods

Glacier surface velocities were estimated using normalized cross-correlation offset tracking. Repeat Sentinel-1A SAR images were employed to generate a time-series of glacier surface velocity maps (Table S1). ERS-1/2, ALOS-1/PALSAR and Envisat/ASAR data were also employed to generate historical surface velocities using the offset tracking method of the GAMMA software.

Annual glacier surface elevation changes were estimated using the geodetic method based on the SRTM DEM, TerraSAR-X/TanDEM-X (TSX/TDX) images and ZiYuan3-02 (ZY3-02) stereo images.

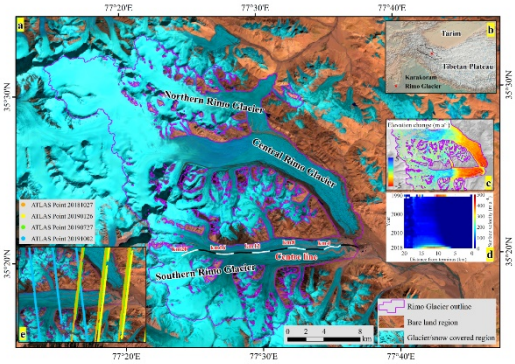

Fig. 1. (a) The outline of the Rimo Glacier. (b) The location of the Rimo Glacier in the Karakoram. (c) Surface elevation changes in the SRG during 2000 – 2016 from Brun et al., 2017. (d) Surface velocities along the center line of SRG during 1990 – 2018 from published dataset. (e) The Ground Track points of ICESat-2 ATL06.

Results

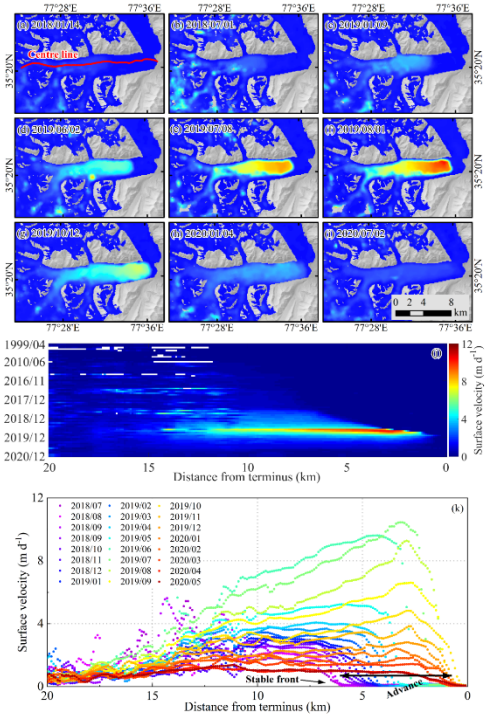

Fig 2. (a-i) Temporal evolution of surface velocities from January 2018 to July 2020 derived from Sentinel-1. (j) Evolution of surface velocities during 1999 – 2000 along the center line of SRG. (k) Annotated time-series of surface velocities vs. distance from the terminus along the center line of SRG.

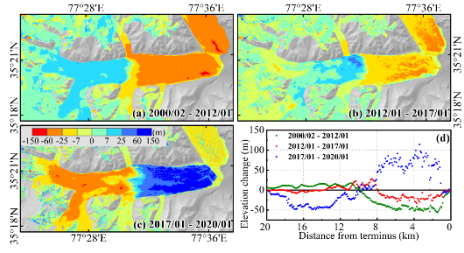

Fig 3. (a-c) Surface elevation changes in the SRG during 2000 – 2012, 2012 – 2017 and 2017 – 2019, respectively, from SRTM, TerraSAR-X/TanDEM-X and ZY3-02 images. (d) Surface elevation changes during the three periods along the center line of SRG.

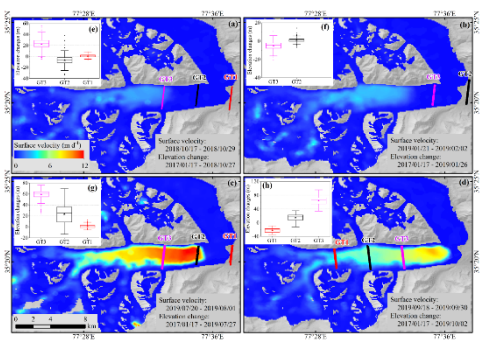

Fig 4 Surface elevation changes from ICESat-2 ATL06 data and TanDEM, and surface velocities in corresponding time. (a-d) Surface velocities in the SRG in October 2018, January 2019, July 2019 and September 2019. (e-h) Surface elevation changes along the Ground Track of ICESat-2 ATL06 during January 2017 – October 2018, January 2017 – January 2019, January 2017 – July 2019, January 2017 – September 2019.

Conclusions

This study characterized the surging dynamics of South Rimo Glacier (SRG) during 2018–2020. The surface velocity is interpreted to have been dominated by ice deformation during the quiescent phase; the glacier base the evolved from cold to temperate with increasing ice thickness and surface slope during the interim phase; surface velocity accelerated and decelerated with the advance of surge front during the active phase. The evolution of the latest SRG surge was probably triggered by the thermal switch, and promoted by hydrological processes. And a surge return period of around 25-30 years was estimated, which is notably longer than for other recently reported surges in this region. Results from this study add to our growing understanding of the surge mechanisms and return periods of Karakoram glaciers.

桂科 AA20302022-1
桂科 AA20302022-4

DBAR-23

2021年可持续发展大数据国际论坛
International Forum on Big Data for Sustainable Development Goals
2021/9/6-8 中国 · 北京

Downscaling of China ASEAN Regional GPM data based on GWR Model

Ning Zhao[1], Yubao Qiu[2*], Guoqiang Jia[2], Xiyan Sun[1]

[1] Guilin University of Electronic Science and technology, Guilin, China

[2] Key Laboratory of Digital Earth Science, Aerospace Information Research Institute, Chinese Academy of Sciences, Beijing, China

Abstract

Precipitation is an important part of the earth water cycle, and the acquisition of precipitation data with high spatial and temporal resolution is very important for water-related sciences and management. Compared with the low spatial coverage of gauged observations, satellite-based precipitation data could better and effectively reproduce the spatial pattern of rainfall. However, the application of satellite-based precipitation data still suffers from the low spatial resolution for detailed water resource management. High-resolution precipitation data is of great significance to agricultural production, drought and flood monitoring and prevention. Thus, we proposed a downscaling satellite-based precipitation data in Guangxi and ASEAN regions, where precipitation is rich and water-related disasters are frequent. The geographically weighted regression model (GWR) was used. We tested the downscaling method by using the state-of-art Global Precipitation Measurement (GPM) satellite precipitation product (Level-3 IMERG) as the dependent variable, digital Elevation Model (DEM), Normalized difference vegetation index (NDVI), actual evapotranspiration (AET) and land surface temperature (LST) data as explanatory variables. An example GWR model was established based on precipitation data in 2013. Finally, monthly downscaling GPM precipitation data was proposed in the study area.The downscaling data has a good consistence with the orginal GPM data in space, with an overall error of -0.048738886, and is potential for depicting detailed spatial variations of precipitation in the study area.

Method

The GWR model can be mathematically described as:

$$Y_i = \beta_0(x_i, y_i) + \sum_{k=1}^{p} \beta_k(x_i, y_i) X_{ik} + \varepsilon(x_i, y_i) \qquad i = 1, 2, 3 \cdots, n$$

Regression paramaters were solved by using the following matrix:

$$\beta(x_i, y_i) = (X^T\, w(x_i, y_i)\, X)^{-1} X^T w(x_i, y_i) \mathrm{Y}$$

The Expoential kernel function can be mathematically described as:

$$w_{ij} = exp(-d_{ij} / h)$$

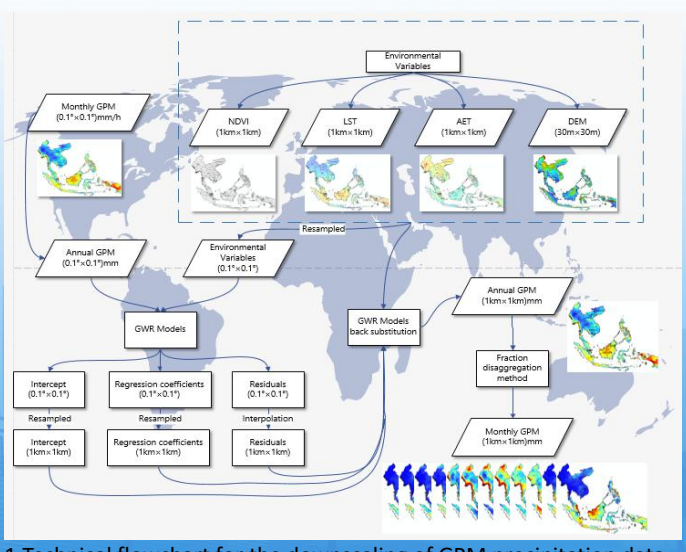

Fig.1 Technical flowchart for the downscaling of GPM precipitation data

Result

The comparison diagram before and after downscaling based on GWR Model is as follows:

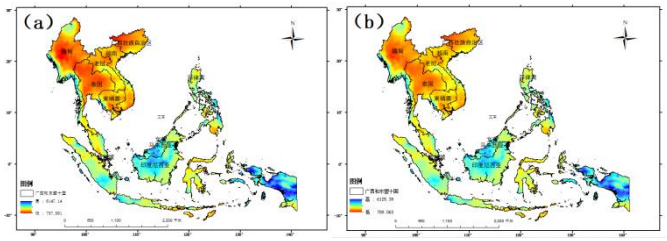

Fig.2 Comparison between the original GPM annual precipitation data (a) and the downscaled data (b).

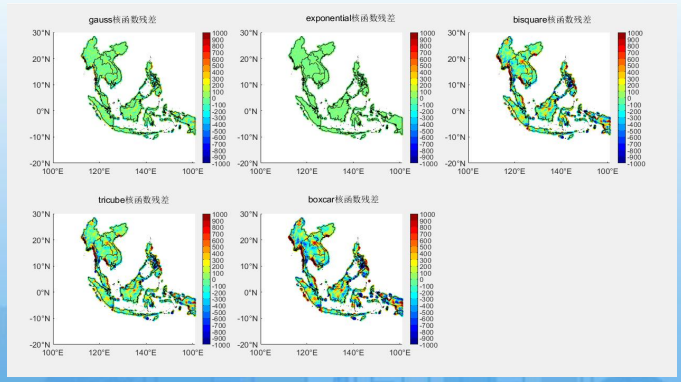

Fig.3 The spatial distribution of errors of GWR models with five different kernels (i.e., Gaussian, exponential, bisquare, tricube and boxcar kernels).

2021年可持续发展大数据国际论坛
International Forum on Big Data for Sustainable Development Goals
2021/9/6-8 中国 · 北京

Land Cover Classification of High Resolution Remote Sensing Image Using Deep Learning Method

Qingting Li

Airborne Remote Sensing Center, Aerospace Information Research Institute, Chinese Academy of Sciences, Beijing 100094, China

Abstract: Land cover and land use information is very important for urban planning, regional management, environmental monitoring and other geospatial applications. A large number of high spatial resolution satellite remote sensing images can be used for land cover mapping. However, the improvement of spatial resolution also increases the complexity of spectral and texture features of ground objects, and the difference of data caused by different image acquisition conditions increases, which brings challenges to land cover classification based on high-resolution images. In recent years, deep convolution neural network has been applied to remote sensing information extraction, and demonstrated the ability of target classification.

Key words: Land cover, remote sensing, high spatial resolution, deep learning, semantic segmentation

1. Objective

In this paper, we studied the land cover information extraction technology based on high-resolution data and deep learning，aiming at the problem of automatic land cover classification with high resolution in large area, based on the needs of deep learning and high resolution remote sensing data for land cover information extraction,

2. Method

The technical process of this paper mainly includes data preprocessing, sample making, network training and optimization, model prediction and accuracy evaluation. Data preprocessing includes image download and selection, radiometric calibration, orthophoto correction, image fusion, image mosaic and image cutting. The sample data set was interpreted by visual interpretation and manual drawing. After the interpretation of the sample area is completed, the field investigation of the remaining area and the establishment of a complete sample database of the study area are carried out, and the interpretation mark database is established according to the sample area and the field survey sample point database. At the same time, the attribute database is established to form the preliminary vector interpretation results.

In this paper, ResUNet was selected as the land use classification network. Compared with the symmetric coding and decoding structure of the ordinary UNet, ResUNet uses ResNet in encoder selection, while the decoder retains the structure of UNet. In this paper, resnet-50 is used as the basic network of reset. Based on pytorch framework, the input slice size is 512, and the learning rate is increased from 1e-5 to 1e-3 by warmup strategy in the first 10 epochs, and then the step learning rate strategy is adopted. In order to enhance the generalization ability of the model, this paper uses a variety of data enhancement methods, such as random HSV color jitter, random rotation, random flip, random blur, random scaling and so on. The pixel overall accuracy and F1 score are used to evaluate the overall classification accuracy and single class classification accuracy of

Table 1 The accuracy assessment of land cover classification

	林地 Woodland （%）	草地 Grassland （%）	湿地 Wetland （%）	耕地 Farmland （%）	人工表面 Artificial surface （%）	其他 Others（%）
Accuracy	87.54	82.75	86.34	89.35	90.76	78.35
Recall	85.97	81.64	84.56	90.72	89.40	76.12
F1 Score	86.75	82.19	85.44	90.03	90.07	77.2
Average F1 Score：85.28%						
Overall classification accuracy：88.27%						

4. Conclusion

In this paper, the deep learning method is used for the classification of land cover, and the high classification accuracy is obtained. The model of land cover classification based on deep learning can be applied to the extraction of land cover information in Henan Province. However, the first class of land cover were just classified in this paper. The classification of secondary class of land cove need to be studied in the future.

classification results.

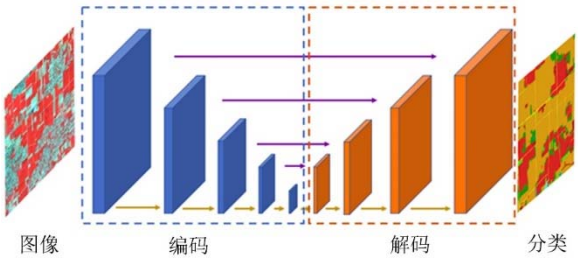

Fig.1The diagram of Network structure

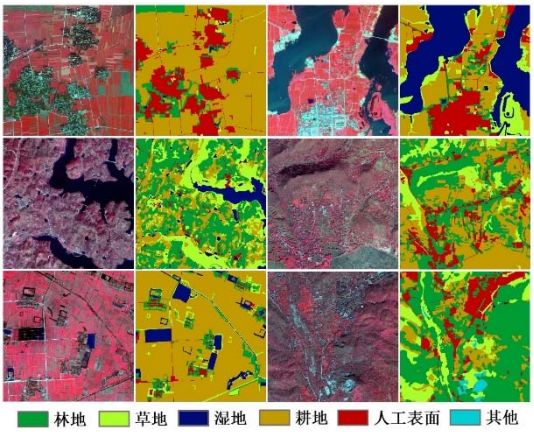

Fig.2 The examples of the training samples

3. Result

The results of land cover classification in Zhengzhou City (including counties and cities under the jurisdiction of the city) show that the overall classification accuracy is more than 88%. The classification accuracy of woodland, wetland, cultivated land and artificial surface is higher, and the classification accuracy of grassland and other types is slightly lower, which may be caused by the confusion of grassland and woodland, and the confusion of bare soil and artificial surface. Villages, roads, ponds and so on can be accurately extracted. It can be seen from the classification results that the woodland of Zhengzhou City (including counties and cities under the jurisdiction of the city) is mainly distributed in the western mountainous area, and the cultivated land is mainly distributed in the eastern plain, reflecting the impact of topography on land cover. The artificial surface area of Zhengzhou City (excluding counties and cities under the jurisdiction of the city) accounts for the majority of the artificial surface of the whole study area, which reflects the position of Zhengzhou as the capital of Henan Province and the central city of central China. Zhongmu County has the largest proportion of cultivated land, and Gongyi City and Dengfeng City have a large proportion of forest land.

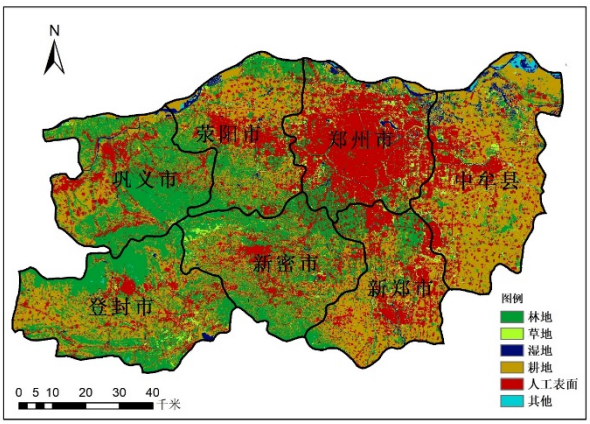

Fig.3 The land cover classification result of Zhengzhou in 2017 with 2 m resolution

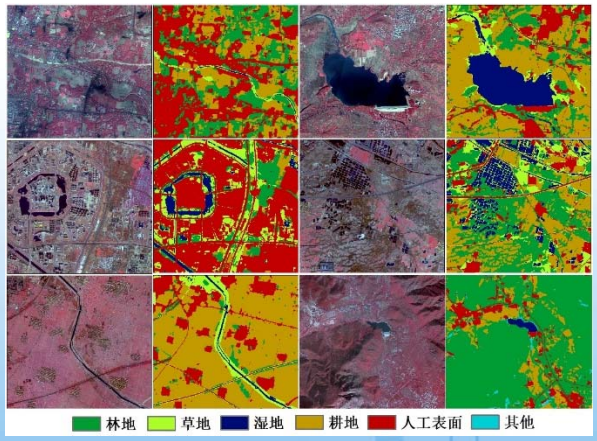

Fig.4 The examples of the land cover classification result of Zhengzhou

DBAR-28

2021年可持续发展大数据国际论坛
International Forum on Big Data for Sustainable Development Goals
2021/9/6-8 中国·北京

Influence of Gas Flaring on Vegetation Changes in Siberia Area

Feng Xiahou[1,2], Yubao Qiu[1]*, Gongwen Wang [2], Qinghuan Li[1]

1. Aerospace Information Research Institute, Chinese Academy of Science (AIR-CAS), Beijing, China
2. School of Earth Sciences and Resources, China University of Geosciences, Beijing 100083, China;

Abstract

The Arctic is rich in oil and gas resources, and is one of the regions with the greatest oil production potential in the world. As global warming and technological advancement, the oil and gas production has increased in Arctic. The Arctic environment is changing and vegetation is turning green. It was widely believed that the change was caused by natural factors such as temperature rising, the impaction of human activities such as gas flaring on vegetation remain poorly understood. Here we selected two major oil and gas development areas in Siberia region of Arctic: Timan-Pechora basin and West Siberia basin, where with a mass of gas flaring. We extract the vegetable, temperature and precipitation information, get the changes of different distances between gas flaring sites and natural growth sites. Compared the growth and changes of vegetation near gas flaring sites and natural sites, analyzed the correlation between the vegetation change characteristics, temperature changes and precipitation .Research show that: Within 0-3km of gas flaring point, the vegetation changes rapidly, which is significantly affected, and vegetation grows better than beyond a certain range compared to nature sits; Flaring points generally have higher temperatures and precipitation than natural points due to gas flaring; gas flaring could increase temperatures and precipitation be higher in area, to promote vegetation to grow more productive.

Background

The Arctic is rich in oil and gas resources. The US Geological Survey's oil and gas resource assessment in the Arctic shows that there is 13% of global oil resources and 30% of natural gas. The Arctic is warming faster 2-3 times than any other region on Earth. The vegetation show widespread greening and partial browning in arctic, the species distribution ranges change rapidly(Beamish et al., 2020). However, the Arctic environment and ecosystem, which is fragile, with a lower ability to recover. Increasing oil and gas exploration activities would cause damage to the fragile Arctic environment (Yu et al., 2015).

Previous studies mostly focused on petroleum basins to study the changes in the wide area, lack of accurate positioning of the research changes. The impaction of human activities such as gas flaring on vegetation remain poorly understood (Seiyaboh et al., 2017). The gas flaring point could effectively locate oil and gas, and indicate the intensity of oil and gas development. Vegetation is an indicator that is sensitive to oil and gas development, could absorb pollutants more than soil. To study the change characteristics of the environment in the Arctic oil and gas region and the mechanism of gas flaring affect vegetation growth, we select gas flaring as sample to explore the question

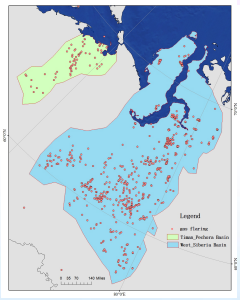

figure 1. Study areas and gas flaring

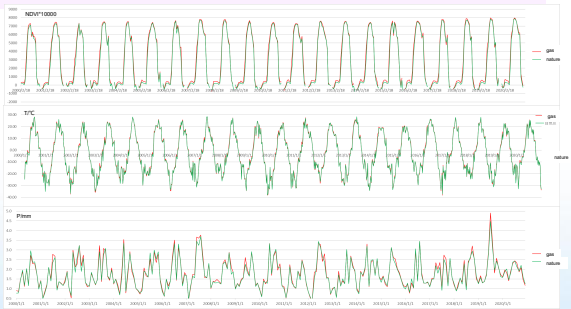

figure 2. NDVI, temperature and precipitation changes in Timan-Pechora basin

Data and methods

Timan-Pechora basin and West Siberia basin, where with a mass of gas flaring, are the main petroleum basins in Siberia Area(figure 1). We use Petroleum Dataset v. 1.2 as the basis to determine the boundary of the study area. We extract the vegetable information from Terra Moderate Resolution Imaging Spectroradiometer (MODIS) Vegetation Indices (MOD13Q1) dataset , temperature information from MODIS Land Surface Temperature/Emissivity (MOD11A2) dataset and precipitation information from ERA5-Land monthly averaged dataset, from 2000 to 2020.

natural evolution points that are less affected by man-made and gas flaring point extracted from Global Gas flaring map 2019, as samples to study. Buffer analysis is performed on natural points and gas flaring points every 1km, and obtain the average value in the area.

Analyze the time series(figure 2) , difference analysis between natural points and gas flaring. The NDVI difference(ΔNDVI) , temperature difference(ΔT), precipitation difference (ΔP), and distance(D) are analyzed for Spearman correlation (figure 3). We selected some natural points in as controls group

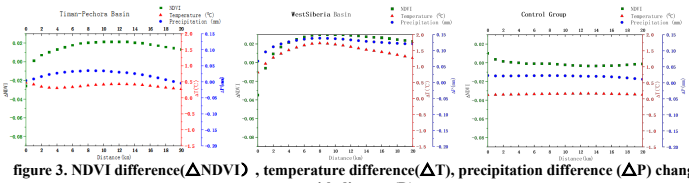

figure 3. NDVI difference(ΔNDVI) , temperature difference(ΔT), precipitation difference (ΔP) changes with distance(D)

Result

From the changes of NDVI, temperature and precipitation, and the correlation analysis. We found:

- The vegetation in the area turns green, and the maximum NDVI gradually increases each year; the temperature increases, and the minimum temperature in winter shows an upward trend; precipitation also shows an upward trend, but the instability becomes stronger;
- Within 0-3km of gas flaring point, the vegetation changes rapidly, which is significantly affected by gas flaring, and the influence gradually becomes weaker as the distance increases;
- The three trends of ΔNDVI, ΔT and ΔP are consistent, their increase with distance, reaches the maximum difference around 9km, and then decreases with distance;
- The differences between gas flaring and natural point in the study area, ΔNDVI&ΔT, ΔNDVI&ΔP are significantly positively correlated, ΔP&D are significantly negatively correlated, ΔP&ΔT is positively correlated.

Type / Regions	ΔNDVI&D	ΔNDVI&ΔT	ΔNDVI&ΔP	ΔP&D	ΔP&ΔT	ΔT&D
Timan-Pechora	……	++	+	—	+	……
West Siberia	……	++	++	—	++	—
Control Group	-	—	……	—	……	……

Table 1. factor correlation distribution

（+ is mean positively correlated, - is mean negatively correlated, …… is no correlation; double symbol meaning P<0.01, single symbol meaning P<0.05）

Conclusion

The results demonstrate that: the $NDVI_{max}$, temperature and total precipitation are increasing; gas flaring sites could significantly affected vegetation in the 0-3km regions, compared with nature sits, vegetation grow better beyond a certain range; Flaring points generally have higher temperatures and precipitation than natural points due to gas flaring; gas flaring could increase temperatures and precipitation be higher in area, to promote vegetation to grow more productive.

This work is support by National Key R&D Program of China (No.2017YFE0111700), and the Strategic Priority Research Program of the Chinese Academy of Sciences, Grant No. XDA19070201.

references

Beamish, A., Raynolds, M. K., Epstein, H., Frost, G. V., Macander, M. J., Bergstedt, & Heim, B. (2020). Recent trends and remaining challenges for optical remote sensing of Arctic tundra vegetation: A review and outlook. Remote Sensing of Environment, 246, 111872.

Yu, Q., Epstein, H. E., Engstrom, R., Shiklomanov, N., & Strelestskiy, D. (2015). Land cover and land use changes in the oil and gas regions of Northwestern Siberia under changing climatic conditions. Environmental Research Letters, 10(12), 124020.

Elvidge, C. D., Zhizhin, M., Baugh, K., Hsu, F. C., & Ghosh, T. (2016). Methods for global survey of natural gas flaring from visible infrared imaging radiometer suite data. Energies, 9(1), 14.

Seiyaboh, Enetimi Idah, and Sylvester Chibueze Izah. "A Review of impacts of gas flaring on vegetation and water resources in the Niger Delta region of Nigeria." International Journal of Economy, Energy and Environment 2.4 (2017): 48-55.